

# NUMERICAL TOOLS FOR CONTRA-ROTATING OPEN-ROTOR PERFORMANCE, NOISE AND VIBRATION ASSESSMENT

**M. Laban, J.C. Kok, B.B. Prananta**  
**National Aerospace Laboratory NLR, Amsterdam, the Netherlands.**

**Keywords:** *Contra-Rotating Open-Rotor, CFD, CAA, FEM*

## Abstract

*Increasing the by-pass ratio of turbofans was successful in the past decades to increase the propulsive efficiency. The ultimate in this sense is the Contra-Rotating Open-Rotor (CROR) which offers a potential of 20% fuel burn reduction relative to classical turbofan engines in service today. Mitigating the inherent noise & vibration issues associated with this propulsion concept, calls for high-fidelity analysis tools. This paper highlights the development of CFD/CAA/FEM-based tools to address these issues.*

## 1 Introduction

The aeronautical industry faces the challenge to counter the environmental impact due to the growth of air transport with low fuel burn innovative products. The Advisory Council for Aeronautical Research in Europe (ACARE) sets a 50% CO<sub>2</sub> emission reduction target for the year 2020. The past decades have shown a gradual increase of the by-pass ratio of turbofan engines which was a successful measure working towards this goal. However, the growth of the by-pass ratio is accompanied by larger and heavier nacelles. At a certain point, the associated nacelle weight increase and drag penalty outweighs the growth in propulsive efficiency. The Contra-Rotating Open-Rotor (CROR) offers a breakthrough. Operating without the drag&weight penalty of a large nacelle, the by-pass ratio is no longer a limiting factor. Operating two contra-rotating



**Fig. 1** Potential 2020 transport aircraft layout featuring a T-tail configuration and CROR in pusher configuration.

"stages" allows to eliminate swirl losses inherent to the classical "single-stage" propeller. The Contra-Rotating Open-Rotor can achieve propulsive efficiencies of 85% at cruise conditions. This offers a potential of 20% fuel burn reduction relative to classical turbofan engines in service today.

Operating without a nacelle, the open-rotor is intrinsically noisier than a turbofan at equivalent thrust setting. The interference between the two rotor stages introduces rotor interaction tones unknown for the classical single-stage propeller. For tail-mounted pusher configurations, see Figure 1 for an illustration, the pylon wake inflow into the rotor again presents an additional noise source.

Experimental and operational CROR's in the USA and Russia have shown that noise and vibration levels of these propulsion devices are critical indeed. Hence, the fuel burn reduction potential is in conflict with another ACARE target: 50% reduction on perceived noise levels by the year 2020.

This paper describes how FEM/CFD/CAA-based numerical tools, combined with massively parallel computing, can be configured towards the analysis of CROR concepts. Applications of these tools to generic rotors are included to illustrate how far field sound pressure levels, rotor vibrations, rotor blade loads, and rotor propulsive efficiency can be computed. With these tools available, potential noise & vibration reduction strategies can be assessed numerically.

## 2 The Computational Fluid Dynamics Model

Rotor loads, vibrations and acoustics find their source in the aerodynamics of the rotor. A Contra-Rotating Open-Rotor shares some basic features with the classical propeller, for which various numerical techniques do exist. However, it is the vortex and viscous wake interaction between the pylon and the rotors and between the front-rotor and the aft-rotor which make the picture more complex. A representation of the physical phenomena specific to a Contra-Rotating Open-Rotor requires to propagate the (tip) vortices and viscous wakes through the various rotor stages.

Although it is quite well possible to extend existing propeller codes, e.g. based on lifting-line or lifting-surface theory, to tackle this challenge, the authors have chosen to apply Computational Fluid Dynamics (CFD) techniques.

### 2.1 Modeling Options

The various parts of the geometry (pylon, first-rotor, second-rotor) have their own rotation direction & velocity. This can be handled by decomposing the geometry in three separate domains. Between the domains, the flow solver data trans-

fer can be setup by means of *Sliding Interfaces* [1]. Two options now present themselves:

- Solve the flow around a single front and a single aft rotor blade by means of steady-state computations in each *Rotating Reference Frame*. Apply periodic boundary conditions on the domain side faces to model the effect of the neighboring blades in the same rotor stage. Apply data averaging in azimuth direction over the sliding interfaces to couple the two rotor domains.
- Expand the single blade numerical meshes to a full rotor stage. Solve the flow in time-accurate mode, in which the front and aft rotor meshes are rotated at each time step. Apply spline-based data interpolation over the sliding interfaces to couple all three domains.

The first modeling option is essentially a steady-state solution which retains some averaged flow features of the rotor only. The *Sliding Interface* between the two rotor stages now functions rather as *Averaging Interface* which effectively smears out the viscous and vortical wakes between the rotor stages. This approach offers very short problem turn around times and can be useful e.g. for a quick view of the rotor propulsive performance. Yet, this approach does not fully address the issues specific to Contra-Rotating Open-Rotors.

The second option allows for a characterization of the rotor physics at a fairly complete level. The vortical and viscous wake interaction between the rotor stages can be retained. Also, non-uniform inflow into the rotor (e.g. due to a pylon) can be modeled. However, this comes at the cost of a high computational effort demanding parallel computing to keep problem turn-around times acceptable.

### 2.2 Grid Generation

Computational Fluid Dynamics computations are performed on multi-block boundary-conforming structured grids. The grids feature three individ-

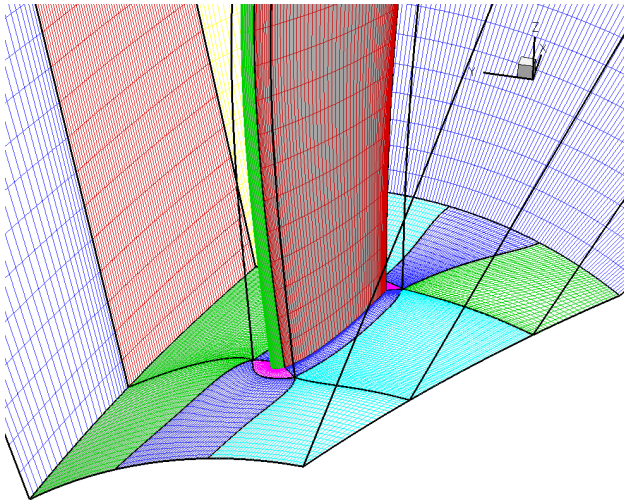


**Fig. 2** Details of the multi-block grid near the rotor blade root at the fine grid level.

ual domains (far-field, first-rotor, second-rotor) that form non-overlapping sliding grids.

A dedicated algorithm is build to automatically wrap an O-O block topology around a rotor blade. In this process, the blade number, blade row spacing and blade pitch angle are taken into account to arrive at optimally shaped block edges. Automating this process holds the advantage that blade pitch angle changes can be accommodated without requiring manual effort.

Grid density and stretching factors are set parametrically along all block edges. This needs to be done manually once for a representative rotor blade. These settings are stored and applied to all subsequent rotor blade variants. Grid dimensions along the block edges are typically a multiple of 8, such that a sequence of sub-level grids are available. In practice, three grid levels (fine, medium, coarse) are used with respectively  $640 \cdot 10^3$ ,  $80 \cdot 10^3$  and  $10 \cdot 10^3$  cells per blade domain. Figure 2 provides an example.

For time-accurate computations, the individual blade grids are copied and rotated to form a full rotor stage. The outer-domain, containing e.g. a pylon or even the complete airframe, is handmade and connects to the sliding interface boundaries of the rotor domains. Figure 3 shows a domain decomposition around the *Smart Fixed Wing Aircraft* project's Contra-Rotating Open-

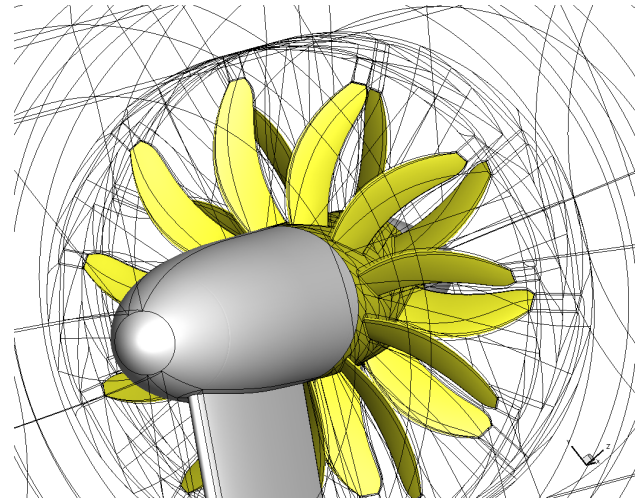


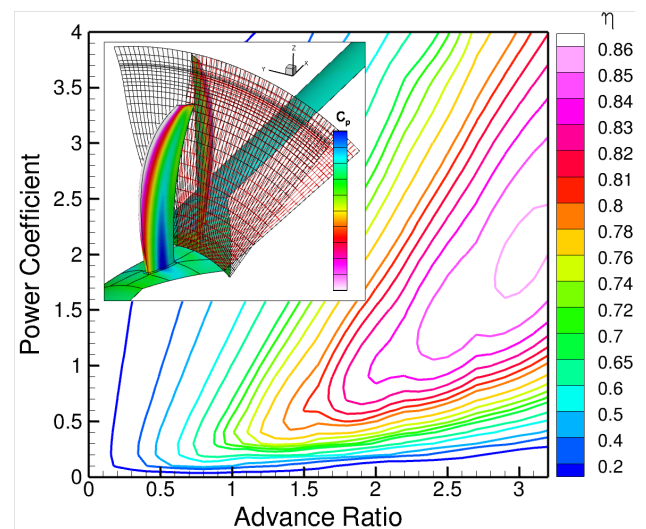
**Fig. 3** Multi-block topology around the SFWA-CROR wind-tunnel test rig.

Rotor wind tunnel test rig. The grid features a total of  $38 \cdot 10^6$  cells on the finest grid level.

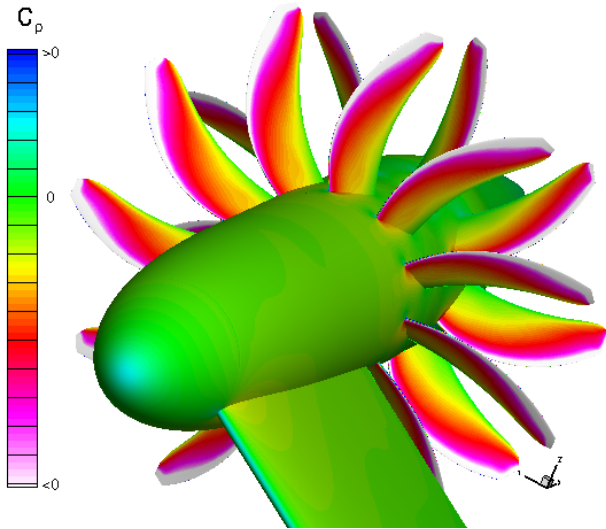
### 2.3 Flow Solver

The CFD computations are based on the Reynolds-Averaged Navier-Stokes (RANS) equations combined with an explicit algebraic Reynolds stress turbulence model [5, 2].

#### 2.3.1 Rotating Reference Frame Solutions



**Fig. 4** CROR propulsive efficiency map computed using the rotating reference frame solution technique.



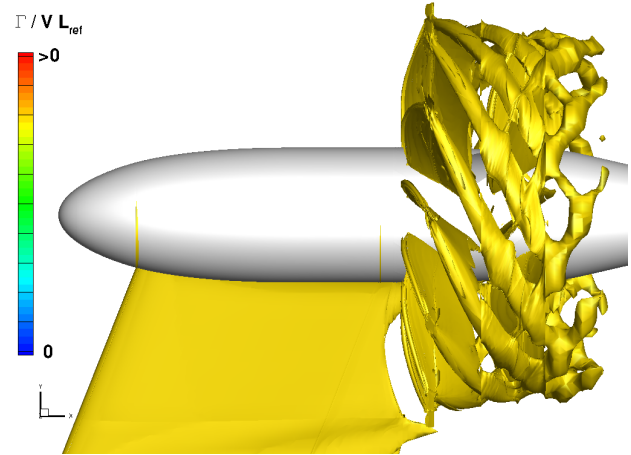
**Fig. 5** SFWA-CROR surface pressure distribution computed with the time-accurate full-rotor solution technique.

Figure 4 provides an example of a solution of the Navier-Stokes equations in the rotating reference frame for the front & aft rotor blades in which an azimuthal data averaging is performed over the sliding grid interface. The rotor performance map shown in Figure 4 is based on computations for multiple blade angle settings. Engineering accuracy can be obtained on the medium grid level for which problem turn around times are in the order of 10 minutes per data point.

### 2.3.2 Time-Accurate Full-Rotor Solutions

Figure 5 provides an example of the time-accurate full-rotor solution technique. A fourth order accurate finite-volume scheme [4] is used to solve the RANS equations. This scheme is dispersion-relation and symmetry preserving, resulting in low numerical dispersion and dissipation. Such properties are essential to capture the rotor-rotor interaction effects which result from the shed front rotor vortical & viscous wakes. Figure 6 shows an example of the propagation of trailing vorticity computed at the medium grid level ( $5 \cdot 10^6$  cells).

The temporal resolution is tuned to the spatial grid resolution over the sliding grid interfaces. For medium grid computations this results in a time step equivalent to a rotor blade azimuth rota-



**Fig. 6** Iso-vorticity contours showing the spatial propagation of trailing vorticity shed by the rotor blades.

tion step of  $0.5^\circ$ . A number of full rotor rotations are required before the solution becomes periodic. The computational load of this approach is relatively high, about 10 days of computing per rotor revolution at the medium grid level employing 8 CPU cores working in parallel. Note that computations at the fine grid level, which is actually required for a sufficient resolution of the rotor physical phenomena, would increase the computational load with a factor of 16.

### 2.3.3 Computing Hardware

Capturing the rotor physical phenomena by means of time-accurate full-rotor CFD is computationally expensive. This calls for applying massively parallel computing platforms. On a Silicon Graphics Altix ICE computing server with 512 CPU cores, the turn-around time of a full-rotor computation at the fine grid level is expected to be one week.

## 3 The Computational Aero Acoustics Model

A number of specific acoustic sources can be identified for a Contra-Rotating Open-Rotor. The approach taken by the authors concentrates on a subset only, namely tonal noise originating from the steady and unsteady pressures acting on the

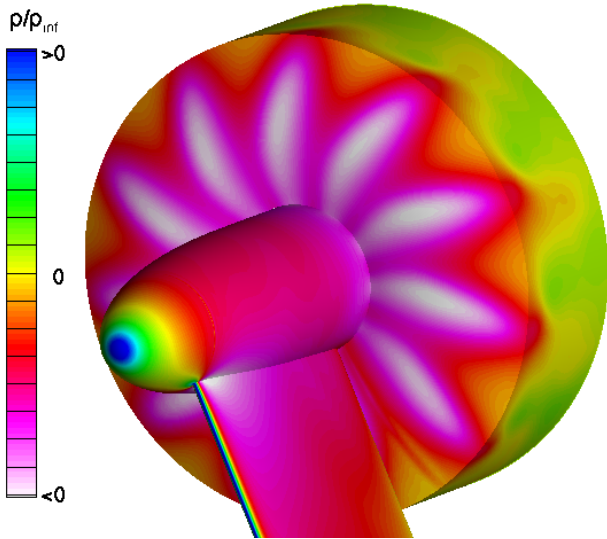


**Fig. 7** Kirchhoff surface keeping a certain distance to the two rotors of the pylon/centre-body mounted SFWA-CROR showing the instantaneous pressure distribution.

rotating blades. This approach includes the so-called *rotor alone tones*, complemented with *interaction tones* which result from blade pressure variation due to pylon-to-rotor and rotor-to-rotor vortical & viscous wake interactions. Also included is the sound wave propagation through the non-uniform flow in the direct vicinity of the rotor blades where high gradients in the flow velocity persist. Shielding and reflections by the engine cowl and pylon potentially affect the acoustic source directivity and are accounted for. However, as soon as the sound waves leave the immediate vicinity of the rotor, a straightforward propagation through uniform flow to the far-field is assumed.

Currently not included is broadband noise originating from the core engine intake and exhaust as well as broadband noise due to turbulent boundary layers. Hence, the current acoustic prediction will underestimate the actual rotor noise.

### 3.1 The Sound Source

The time-accurate CFD solution, described in Chapter 2, contains both the sound generation and the propagation of the sound through the non-uniform flow field in the immediate vicinity

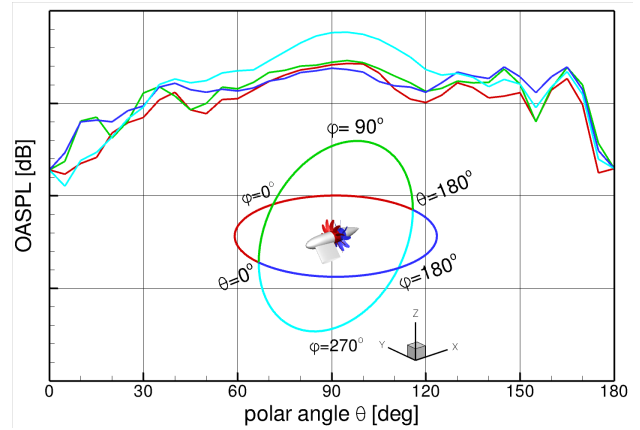


**Fig. 8** Far field overall sound pressure level and directivity.

of the rotor. Sound waves are captured accurately by employing a fourth-order finite-volume scheme with low numerical dissipation and dispersion. The maximum frequency content is determined by the temporal (CFD time step) as well as the spatial discretisation (CFD grid cell spacing). As a rule of the thumb, a minimum of 8 grid cells per wave length are deemed necessary to propagate a sinusoidal sound wave. Therefore the CFD mesh size needs to be relatively small in the region around the rotor and the surfaces (nacelle & pylon) which are to be taken into account for shielding/reflecting.

### 3.2 Sound Propagation to the Far Field

A direct approach in which CFD carries the sound waves all the way to the far field is both prohibitively expensive and unnecessary. CFD meshes tend to loose resolution when approaching the far-field and this will cause the sound waves to dissipate numerically. Also, the flow soon becomes quite uniform so that the wave propagation does not require relative "expensive" solutions of the Euler equations. A practical approach is to wrap a closed surface, a so-called *Kirchhoff surface*, around the rotor on which to extract the flow variables (pressure and pressure gradient) as function of time. A Kirchhoff integral method in the frequency domain is used to compute the sound propagation from the Kirchhoff surface to any desired location in the far

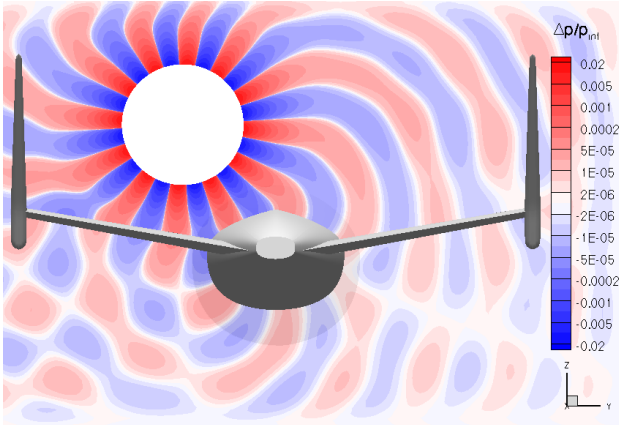


**Fig. 9** Front rotor tone pressure waves propagating over NACRE's noise shielding U-tail.

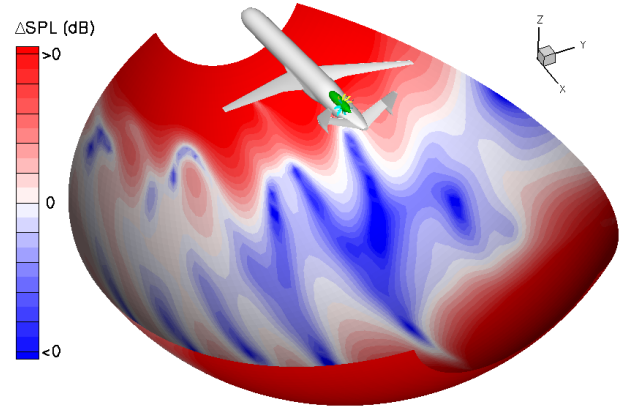
field.

Figure 7 illustrates the Kirchoff surface around a pylon/centre-body mounted CROR. For this application, part of the Kirchoff surface coincides with the sliding mesh interface used by the CFD solver to exchange information between the rotating and stationary flow domains. Figure 8 shows the corresponding far field overall sound pressure levels as function of polar angle.

### 3.3 Accounting for Airframe Shielding Surfaces

Depending on the aircraft configuration, acoustic shielding and/or reflection due to the airframe surfaces can have a significant impact on the perceived far field noise levels. If these need to be incorporated in the acoustic analysis, an intermediate modeling technique can be placed "in between" the full time accurate Navier-Stokes model around the rotor (Section 3.1) and the Kirchoff surface from which the data is extrapolated to the far field (Section 3.2). This intermediate model is based on time accurate solutions of the linearized Euler equations using again a fourth-order finite volume scheme as well as a fourth-order Runge Kutta scheme. It does require a volumetric meshing of the 3D space around the airframe. The mesh is boundary conforming and preferably isotropic with 8 grid cells per wave length to be propagated.

Figure 9 shows an illustration of a front ro-



**Fig. 10** Effect of NACRE's acoustic shielding U-tail on far field sound pressure levels due to a single frequency front rotor tone.

tor tone propagating over a noise shielding U-tail, computed in the context of EU-project *New Aircraft Concepts REserach* (NACRE). Figure 10 shows the differential effect (shielding) on the far field sound pressure levels.

## 4 The Aeroelastic Model

For maximum propulsive & acoustic performance, rotor blades tend to be very thin. At the same time, the rotor blade inflow is highly distorted due to the pylon & upfront rotor blade wakes that impinge on the downstream blades. This leads to static as well as dynamic rotor blade aeroelastic deformations that can be relatively large and may impact the rotor loads, vibration, performance and acoustic behavior. The aeroelastic effects are taken into account in the CFD model (Chapter 2) through a fluid-structure interaction in modal space [7].

### 4.1 The Blade Finite Element Model

Full-scale flight CROR blades commonly feature a complex structure, comprising a metallic support structure complemented with a carbon fiber laminate skin. Scaled CROR models for wind tunnel experiments usually feature a solid titanium or a solid carbon fiber structure.

The numerical representation of solid metallic CROR blades in Finite Element codes (e.g.

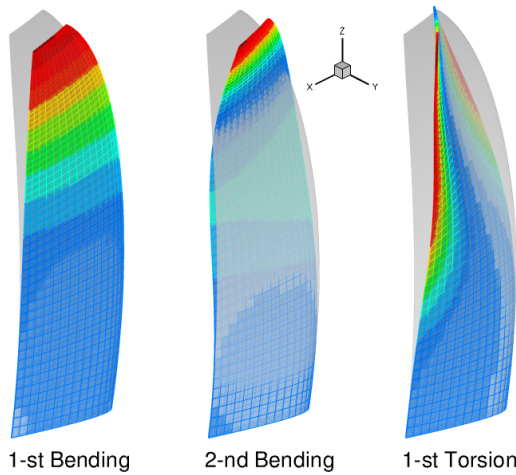


**Fig. 11** FE-computed first three mode shapes of a metallic wind-tunnel model scale rotor blade.

MSC-NASTRAN) is rather straightforward. The blade geometry is meshed using hexahedral (CHEXA) elements. The titanium material is represented with isotropic material property cards (MAT1). The blade root is constraint to the rigid outer world using appropriate boundary conditions (SPC's).

The dynamic properties of a rotating blade are influenced by the centrifugal, the Coriolis and the aerodynamic forces. The centrifugal & aerodynamic forces affect the eigenfrequencies and the mode shapes by the change of the stiffness property due to static deformation of the blades under these forces, i.e. the so-called pre-stressing effect. The Coriolis force introduces damping in the system. The dependency to these forces implies that the eigenfrequencies and mode shapes of rotating blades depend on the speed of rotation. In most cases the eigenfrequencies raise with the increase of speed of rotation leading to a stiffening effect.

To take the pre-stressing effect into account, the computation of the eigenfrequencies and mode shapes starts from a statically deformed state as a function of the speed of rotation. Since the most important effect influencing the eigenfrequencies and the mode shapes comes from the centrifugal force, the aerodynamic force is neglected. The computation of the static deformation due to centrifugal force is carried out using

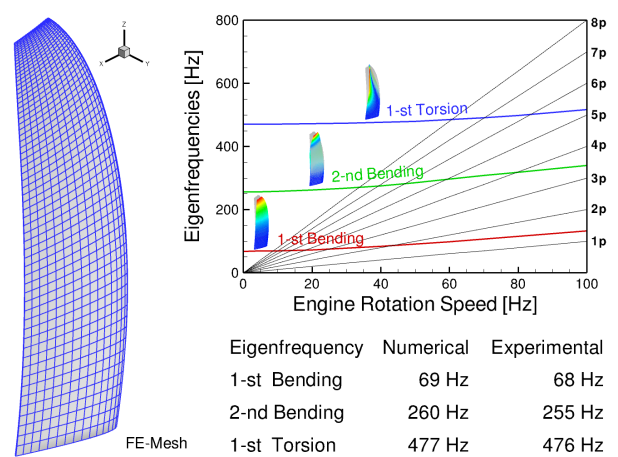


**Fig. 12** The FE-mesh, the numerical versus experimental eigenfrequencies, and the Campbell diagram of a metallic wind-tunnel model scale rotor blade.

the RLOAD card of NASTRAN. The solution is used in a subsequent eigenvalue analysis using special DMAP macros. When damping due to the Coriolis force is included, a complex eigenvalue solver has to be used (SOL107 of NASTRAN), otherwise a real eigenvalue solver can be used (SOL103).

Figure 11 illustrates the FE-computed first three mode shapes (first bending, second bending, first torsion) of a representative titanium wind-tunnel model scale CROR blade. Figure 12 illustrates the computed versus measured ("ping test") eigenfrequencies at zero rotation rate. The numerical predictions match the experimentally measured eigenfrequencies within a few percent margin. The first three eigenmodes are of particular interest as the associated eigenfrequencies usually lay well within the range of potential rotor excitation frequencies due to rotor inflow distortions. This information is presented in a so-called Campbell diagram, Figure 12. It also highlights the centrifugal stiffening effect on the computed eigenfrequencies.

For carbon fiber CROR blades, the finite element modeling is more complex and is subject of research. The current approach is to use anisotropic shell elements (CQUAD4) representing each individual laminate layer. In the near future, the authors expect to have data on the cor-

relation with experimental values to validate this modeling approach.

#### 4.2 Aero-Elastic Coupling with the Flow Solver

To compute the dynamic aeroelastic deformations of the blades, the structural model must be coupled to the CFD flow solver. Given the aerodynamic forces, the structural model determines the dynamic deformations of the blades, which are passed to the flow solver. Given the deformations, the flow solver computes the aerodynamic forces, which are passed back to the structural model. An iterative scheme, based on a prediction-correction method [6], is used to solve this dynamic fluid-structure interaction process. In practice, a small number of iterations is required to obtain sufficient convergence in each time step.

The structural model computes the dynamic deformations in the space spanned by the mode shapes of the blades. The dynamic equations in modal space are driven by so-called generalized aerodynamic forces. This generalized force is obtained by projecting the aerodynamic forces working on the aerodynamic surface on each mode shape. In order to transfer the structural deformations back to the physical space used in the flow solver, the volume spline method [3] is used to deform both the aerodynamic surface grid and the CFD volume grid.

### 5 Conclusions

Massively parallel computing systems have become affordable today. This allows to run a numerical simulation of a Contra-Rotating Open-Rotor which captures all the relevant physical phenomena. This paper illustrated the basic ingredients to setup such an analysis. With the numerical capability in place, engineers can start to address some of the ideas that are currently on the table to reduce the CROR perceived noise levels. If this challenging issue can be solved successfully, the Contra-Rotating Open-Rotor can make a very significant contribution to reduce the envi-

ronmental impact of the future transport aircraft.

#### 5.1 Copyright Statement

The authors confirm that they, and/or their company or organization, hold copyright on all of the original material included in this paper. The authors also confirm that they have obtained permission, from the copyright holder of any third party material included in this paper, to publish it as part of their paper. The authors confirm that they give permission, or have obtained permission from the copyright holder of this paper, for the publication and distribution of this paper as part of the ICAS2010 proceedings or as individual off-prints from the proceedings.

#### 5.2 Acknowledgement

This research is 50% funded by the European Union in the 6-th framework programme *New Aircraft Concepts REsearch* (NACRE), in the 7-th framework programme by the Clean Sky Joint Technology Initiative's *Smart Fixed Wing Aircraft* ITD (Grant Agreement No CSJU-GAM-SFWA-2008-001), and 50% by NLR's programmatic research "Kennis voor Beleid" and "Kennis als Vermogen".

### References

- [1] Boelens O. J, van der Ven H, Kok J. C, and Prananta B. B. Rotorcraft simulations using a sliding-grid approach. *Proc European Rotorcraft Forum 34* ??, 2008.
- [2] Dol H. S, Kok J. C, and Oskam B. Turbulence modelling for leading-edge vortex flows. *Proc 40<sup>th</sup> Aerospace Sciences Meeting & Exhibit*, Reno, Nevada, 14–17 January 2002.
- [3] Hounjet M. H. L and Meijer J. J. Evaluation of Elastomechanical and Aerodynamic Data Transfer Methods for Non-planar Configurations in Computational Aeroelastic Analysis. *Proc Proceedings of 1995 CEAS International Forum on Aeroelasticity and Structural Dynamics*, pp 11.1–11.24, Manchester, June 1995. Royal Aeronautical Society, also NLR-TP-95690, NLR, 1995.
- [4] Kok J. C. A high-order low-dispersion symmetry-preserving finite-volume method for compressible flow on curvilinear grids. *Journal of Compu-*

*tational Physics*, Vol. 228, pp 6811–6832, 2009. NLR-TP-2008-775.

- [5] Kok J. C and Spekreijse S. P. Efficient and accurate implementation of the  $k-\omega$  turbulence model in the NLR multi-block Navier–Stokes system. *Proc ECCOMAS 2000*, Barcelona, Spain, 11–14 September 2000. NLR-TP-2000-144.
- [6] Prananta B. B and Hounjet M. H. L. Large time step aero-structural coupling procedures for aeroelastic simulation. *Proc Proceedings of 1997 CEAS International Forum on Aeroelasticity and Structural Dynamics*, Vol. 2, pp 63–71, Rome, June 1997. Associazione Italiana di Aeronautica ed Astronautica, also NLR-TP-97619, NLR, 1997.
- [7] Prananta B. B, Kok J. C, Spekreijse S. P, Hounjet M. H. L, and Meijer J. J. Simulation of limit cycle oscillation of fighter aircraft at moderate angle of attack. *Proc International Forum on Aeroelasticity and Structural Dynamics*, Amsterdam, the Netherlands, 4–6 June 2003. NLR-TP-2003-526.